

1 SediNet: A configurable deep learning model for mixed qualitative and quantitative optical
2 granulometry

3 Daniel Buscombe

4 Geosciences Division, School of Earth and Sustainability, Northern Arizona University

5

6 Abstract

7 I describe a configurable machine-learning framework to estimate a suite of continuous and
8 categorical sedimentological properties from photographic imagery of sediment, and to
9 exemplify how machine learning can be a powerful and flexible tool for automated quantitative
10 and qualitative measurements from remotely sensed imagery. The model is tested on a large
11 dataset consisting of 400 images and associated detailed label data. The data are from a
12 much wider sedimentological spectrum than previous optical granulometry studies,
13 consisting of both well- and poorly sorted sediment, terrigenous, carbonate, and
14 volcanoclastic sands and gravels and their mixtures, and grain sizes spanning over two orders
15 of magnitude. I demonstrate the model framework by configuring it in several ways, to
16 estimate two categories (describing grain shape and population, respectively) and nine
17 numeric grain-size percentiles in pixels from a single input image. Grain size is then
18 recovered using the physical size of a pixel. Finally, I demonstrate that the model can be
19 configured and trained to estimate equivalent sieve diameters directly from image features,
20 without the need for area-to-mass conversion formulas and without even knowing the scale
21 of one pixel. Thus, it is the only optical granulometry method proposed to date that does not
22 necessarily require image scaling. The flexibility of the model framework should facilitate
23 numerous application in the spatio-temporal monitoring of the grain size distribution, shape,
24 mineralogy and other quantities of interest, of sedimentary deposits as they evolve as well
25 as other texture-based proxies extracted from remotely sensed imagery.

26

27 1. Introduction

28 Sediment grain size fundamentally influences the physics of flows of water, wind, ice and
29 sediment that continually shape landforms. Large sedimentological datasets have led to
30 important discoveries in dynamic environments such as contemporary river beds, sea beds
31 and aeolian sediment surfaces that are constantly changing under fluid power, for example
32 in sediment transport (e.g. *Masteller & Finnegan, 2017; Rubin et al., 2019*), channel bed
33 mobility (e.g. *Montgomery et al., 1999*), channel geometry (e.g. *Pfeiffer et al., 2017*), sediment
34 provenance (e.g. *Paterson & Heslop, 2015*), sediment abrasion (e.g. *Novak-Szabo et al.,*
35 *2018*), hydraulic resistance (e.g. *Rickenmann & Recking, 2011*), particle settling (e.g.
36 *Sternberg et al., 1999*) and dispersal at coasts (e.g. *Wheatcroft & Borgeld, 2000*), and beach
37 dynamics (e.g. *Bergillos et al., 2016*). Traditionally, the means of acquiring large grain size
38 (or shape, or any other metric) data sets has been laborious and time-consuming through
39 laboratory analyses of samples taken in the field. Optical granulometry is the measurement
40 of sediment from statistical analysis of image intensity and texture, and has been driven by
41 instrumental (e.g. *Buscombe et al., 2014; Carbonneau et al., 2018; Rubin et al., 2007;*
42 *Woodget et al., 2018*) and analytical (e.g. *Black et al., 2014; Buscombe et al., 2010;*
43 *Buscombe and Rubin, 2012b; Buscombe, 2013; Cheng and Liu, 2015; Carbonneau et al.,*
44 *2005a, 2005b; Carbonneau et al., 2004; Cuttler et al., 2017; Dugdale et al., 2010; Legleiter*
45 *et al., 2016; Rubin, 2004; Woodget et al., 2017*) developments over the past 15 years.
46 Another set of deterministic methods known as 'photosieving' (e.g. *Adams, 1979*) or object-
47 based image analysis or OBIA (*Carbonneau et al., 2018*) have been developed (e.g. *Detert*
48 *and Weitbrecht, 2012; Graham et al., 2005*) that aim to identify each individual grain and
49 cannot therefore be used on grains smaller than one pixel (subpixel) which is not a theoretical
50 limitation of optical granulometry techniques that statistically quantify image texture

51 (*Carbonneau et al.*, 2004). One major goal of this corpus of work is to develop a reliable suite
52 of techniques for spatio-temporal monitoring of the grain size of sedimentary deposits as they
53 evolve, remotely and automatically. This has the potential to significantly alter the way
54 geomorphological research is carried out (e.g. *Viles*, 2016) and may hopefully lead to
55 significant discoveries in the two-way feedbacks between evolving sedimentary landform
56 morphologies and the spatio-temporal dynamics of grain size, or 'morpho-sedimentary
57 dynamics' (cf. *Buscombe and Masselink*, 2006), at large field scales. This will require
58 measuring grain size at the same spatial (e.g. *Rubin et al.*, 2019) and temporal (e.g.
59 *Buscombe et al.*, 2014) coverage as is now possible with topographic measurements that
60 can capture the spatio-temporal evolution of small-scale morphologies (e.g. *Austin et al.*,
61 2007; *Nield et al.*, 2011; *Turner et al.*, 2008; *Williams et al.*, 2014).

62

63 The present study is motivated by five observations. First, the wavelet-based optical
64 granulometry method of *Buscombe* (2013), while accurate for relatively well-sorted sediment
65 (e.g. *Masteller and Finnegan*, 2017; *Michaelides et al.*, 2018; *Prodger et al.*, 2016; *Smith et*
66 *al.*, 2018), can be inaccurate for images of grains that are poorly sorted such as sand and
67 gravel mixtures, or where there are relatively few individual grains in the image (hundreds to
68 thousands of grains are typically required). For this study, I have collated a dataset of more
69 than 100 images of sediment that mostly fall under these two categories, to augment the 300-
70 image dataset used by *Buscombe* (2013) that contained a greater proportion of relatively
71 well-sorted sediment, in order to develop a more generally applicable method. Some images
72 contain as few as 10 individual grains, whereas others depict millions of individual grains.

73

74 Second, optical granulometry methods quantify the size of apparent axes of grains in the
75 image plane, where many grains may be overlapping. If a bulk (i.e. by mass or by volume)

76 sample size distribution is the information required, the *Buscombe* (2013) or similar method
77 can provide comparable grain size distributions to those derived using sieves or similar
78 methods usually only if the appropriate conversion of area- to mass-by-size is made, which
79 takes the form (*Diplas and Sutherland*, 1988; *Kellerhals and Bray*, 1971):

$$80 \quad p(V - W)_i = \frac{p(A)_i D_i^x}{\sum p(A)_i D_i^x} \quad (1)$$

81 where $p(V - W)_i$ is the volume by weight proportion of the i th size fraction, $p(A)_i$ is the image-
82 derived areal proportion of the i th size fraction, D_i is the grain size of the i th size fraction and
83 x is a conversion constant. See also *Graham et al.*, (2012) for field applications of this
84 conversion. *Diplas and Fripp* (1992) suggest that it is necessary to use different values for
85 exponent x depending on grain size, but *Diplas et al.* (2008) suggest a pragmatic approach
86 is to use an average value for x , which is determined empirically for each population of grains
87 imaged. *Cuttler et al.* (2017) confirmed that x must be determined empirically for bioclastic
88 carbonate sediment to avoid over-predicting sieve sizes and sediment settling velocities from
89 parametric formulas, even though the *Buscombe* (2013) method worked well to estimate the
90 apparent axes of grains from the imagery. Here, I demonstrate that machine learning can be
91 used to map image features to sieve sizes directly, without the need for conversion formulas
92 and without even knowing the scale of a pixel.

93 The third motivation for this study is provided by *Shojiet et al.* (2018) who demonstrated the
94 utility of deep learning techniques to classify volcanic ash particles by shape, and specifically
95 that a well-designed deep convolutional neural network (CNN) can automatically extract the
96 relevant features from imagery of particles to estimate a categorical quantity. Here, that work
97 is extended by demonstrating that the same CNN architecture can be used for both discrete
98 (classification) and continuously varying quantities (regression) from a single image, by
99 estimating categorical particle shape and population, and numerical percentiles of the grain

100 size distribution. CNNs are a type of artificial neural network (ANN) and part of a class of
101 machine learning techniques called deep learning (*Goodfellow et al., 2016*) that have recently
102 been shown to perform well for both classification and regression tasks equally, including in
103 numerous geosciences applications where relevant image features are extracted
104 automatically (e.g. *Buscombe and Carini, 2019; Buscombe et al., 2019; Buscombe and*
105 *Ritchie, 2018; Linville et al. 2019; Luo et al., 2018; Jiang et al., 2018; Reichstein et al., 2019*).
106 The basic premise of applications such as these, compared to those of other machine
107 learning subcategories, is that it circumvents the need (and the effort required) to make
108 decisions about what extracted image features are important to a specific task, which tends
109 to make the models both more subjective and more powerful.

110

111 The fourth motivation is that predictive modeling techniques for both categorical and
112 numerical output quantities in the geosciences is somewhat rare. Categorical variables are
113 those that are ascribed an integer, but where the values themselves do not have a physical
114 meaning as they simply enumerate the possible realizations of a phenomenon. As such, they
115 are limited by our ability to identify and ascribe meaning to the phenomenon, and also as
116 intra-categorical variation approaches inter-categorical variation. However, for trivial, well-
117 known or unambiguously defined quantities, they are an essential part of the geosciences,
118 but whereas some techniques are designed for handling continuous estimates, others are
119 better for handling categorical or discrete variables. This typically requires the development
120 of transforms that convert continuous to categorical (using discretization, dummy variables,
121 etc.), which can be subjective if thresholds or discrete bins need to be defined. Here I describe
122 a single empirical framework that can be trained to predict both categorical and continuous
123 quantities, as needed, which might be useful in other geophysical contexts. Within the
124 framework of an ANN, this is relatively straightforward: essentially, multinomial logistic

125 regression is used for image features that have been distilled by a CNN to estimate discrete
126 variables (such as categorical grain shape), and linear regression for continuous variables
127 (such as grain size). For the latter, the key to the framework is to provide the image features
128 that scale linearly with the response variable (e.g. grain size) being estimated. Highlighting
129 this relatively simple principle through demonstration is worthwhile if it motivates similar
130 progress in other geophysical contexts.

131

132 The final and perhaps foremost motivation to developing yet another optical granulometry
133 technique is the observation that the data-hungry nature of machine learning allows for
134 collaborative tool development for extracting scientific information from images of sediment.
135 Recognizing the variety of both sediment imagery, due to the inherent variability of natural
136 sediment, and potential SediNet applications, the motivating idea behind the creation of the
137 SediNet model and software (*SediNet online software*, 2019) is to foster the creation of such
138 a community. Users can contribute imagery, models, and retrain existing models, as well as
139 using existing SediNet models contained in the repository.

140

141 2. Data

142 The model is trained and tested on a large data set consisting of 400 labeled images of
143 sediment (Figures 1 and 2), with a large variation in the spatial footprint (field-of-view) of each
144 image, the spatial resolution (physical size of a pixel), and variation in camera sensor. The
145 data are from a wide sedimentological spectrum of well and poorly sorted sediment,
146 consisting of terrigenous (derived by erosion of crystalline, volcanic, and sedimentary rocks),
147 carbonate (skeletal grains, oolites, and some locally derived detrital carbonate), and
148 volcanoclastic (lapilli, glass, and pyroclastic bombs) sands and gravels and their mixtures,
149 and grain sizes in pixels spanning over two orders of magnitude. Out of the 400 images, 300

150 were compiled and used by *Buscombe* (2013) to develop a wavelet-based algorithm for
151 estimating grain size from imagery (sets A and C in that paper). The remaining 100 samples
152 were compiled for this study, from various fieldwork activities over more than 10 years in
153 various coastal and riverine environments on several continents. The additional 100 samples
154 were chosen specifically to better represent within the dataset both poorly sorted mixed sand
155 and gravel sediment and (usually microscopic) imagery with relatively few numbers of grains.

156

157 2.1. Grain Size

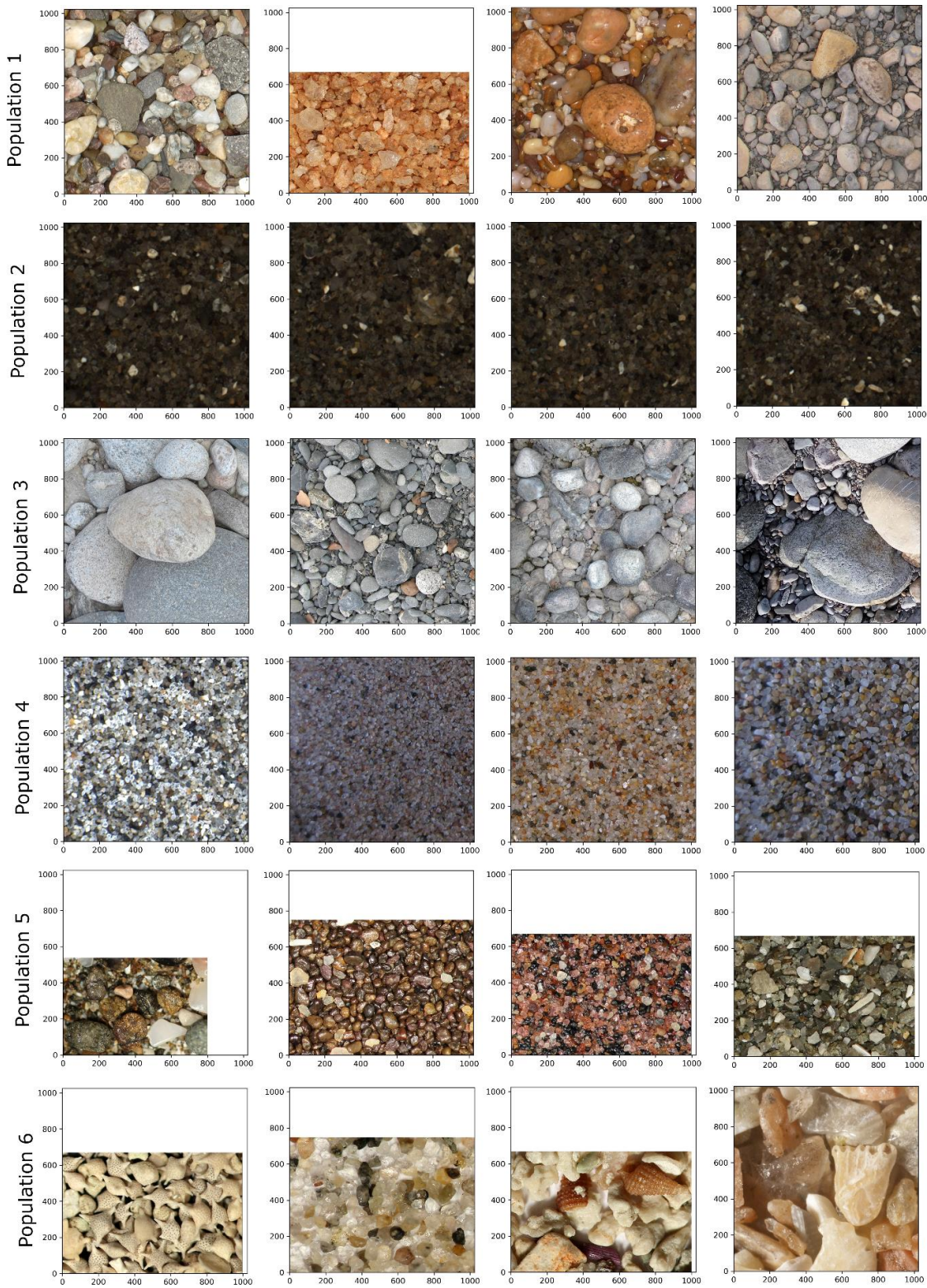
158 The size distribution of intermediate axes of apparent (surface) grains was compiled for each
159 image following the on-screen manual method of *Barnard et al.* (2007), which is the only way
160 in which to reliably obtain a comparable grain-size distribution to that provided by image-
161 based methods (*Baptista et al.*, 2012; *Buscombe et al.*, 2010; *Cuttler et al.*, 2017). However,
162 it is a time-consuming and meticulous process, usually taking a trained operator 30-60
163 minutes per image to measure the axes of up to 500 grains. Nine commonly utilized
164 percentiles of the cumulative size distribution (namely 5, 10, 16, 25, 50, 75, 84, 90, and 95th
165 percentiles) were calculated for each measured size distribution.

166

167 2.2. Grain shape and population

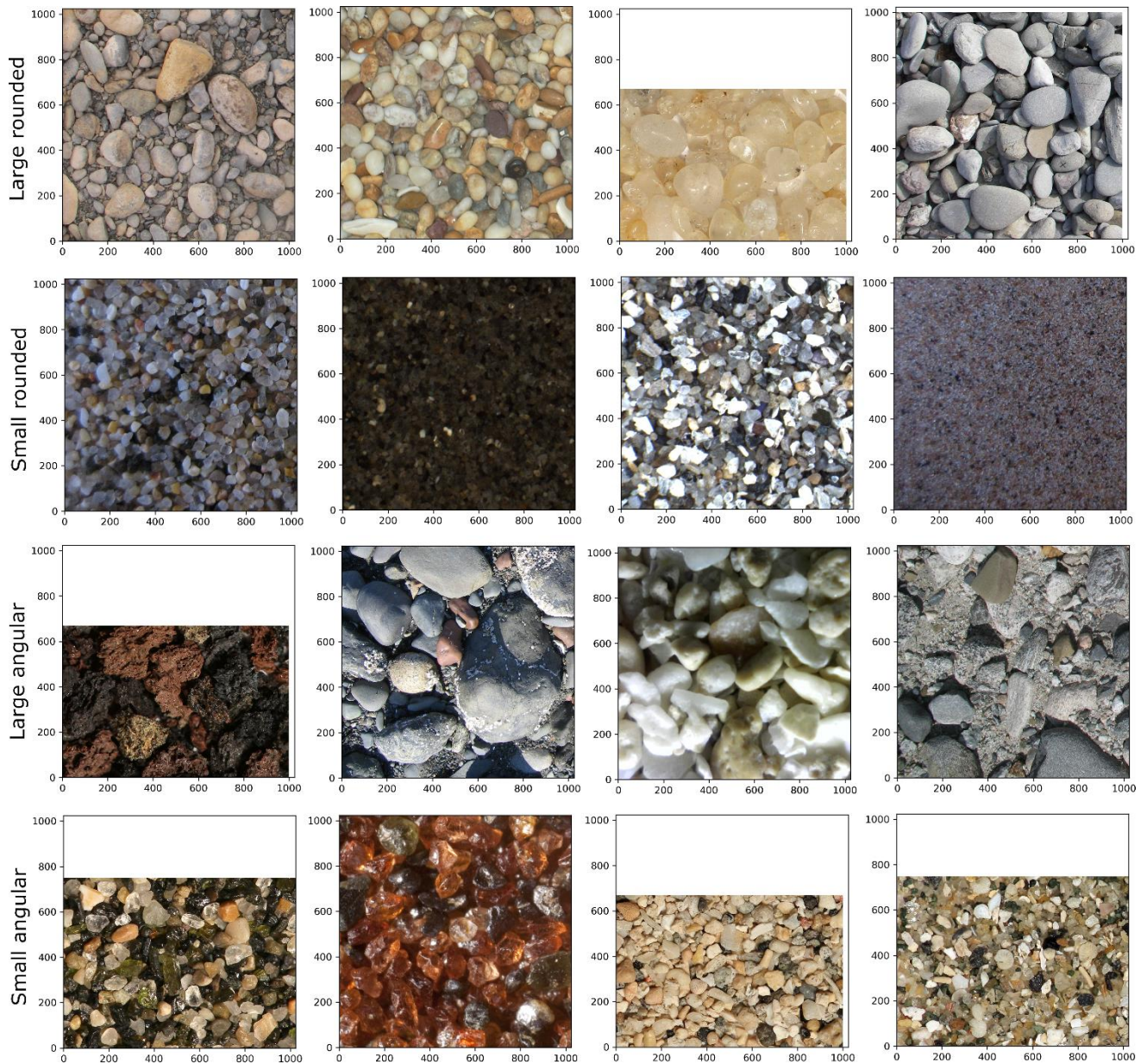
168 The expanded dataset of 400 images contain a number of sediment populations (Figure 1)
169 that I manually grouped into six categories: 1) well-sorted gravel; 2) well-sorted sand and
170 shell hash from underwater camera (described in *Buscombe et al.*, 2014); 3) relatively poorly
171 sorted gravel and sand-gravel mixtures (including imagery from *Warrick et al.*, 2009); 4) well-
172 sorted sand; 5) miscellaneous terrigenous and volcanoclastic grains; and 6) miscellaneous
173 bioclastic (carbonate) grains. Additionally, each of the 400 images were classified into four

174 shape/size categories (Figure 2), namely 1) large well-rounded grains; 2) small well-rounded
175 grains; 3) large angular grains; and 4) small angular grains.



176

177 *Figure 1: Four example 1024 x 1024 pixel subsets of images from each of six population categories. From top to bottom: 1) well-*
178 *sorted gravel; 2) well-sorted sand and shell hash from underwater camera (described in Buscombe et al., 2014); 3) relatively poorly*
179 *sorted gravel and sand-gravel mixtures (including imagery from Warrick et al., 2009); 4) well-sorted sand; 5) miscellaneous*
180 *terrigenous and volcanoclastic grains; and 6) miscellaneous bioclastic (carbonate) grains.*



181

182 *Figure 2. Four example 1024 x 1024 pixel subsets of images from each of four shape categories. From top to bottom: 1) Large well*
 183 *rounded grains; 2) small well-rounded grains; 3) large angular grains; and 4) small angular grains.*

184

185 **3. SediNet model**

186 Deep learning models have multiple processing layers (called convolutional layers or blocks)
 187 and nonlinear transformations (that include batch normalization, activation, and dropout,
 188 which are explained below), with the outputs from each layer passed as inputs to the next.
 189 SediNet (Figure 3) is a supervised deep neural network model framework that can be used
 190 as presented in this paper, or alternatively configured for custom purposes, by training on

191 any number of input images for any number of numeric or categorical outputs. For the
192 purposes of demonstrating the model in this paper, several SediNet models were made:

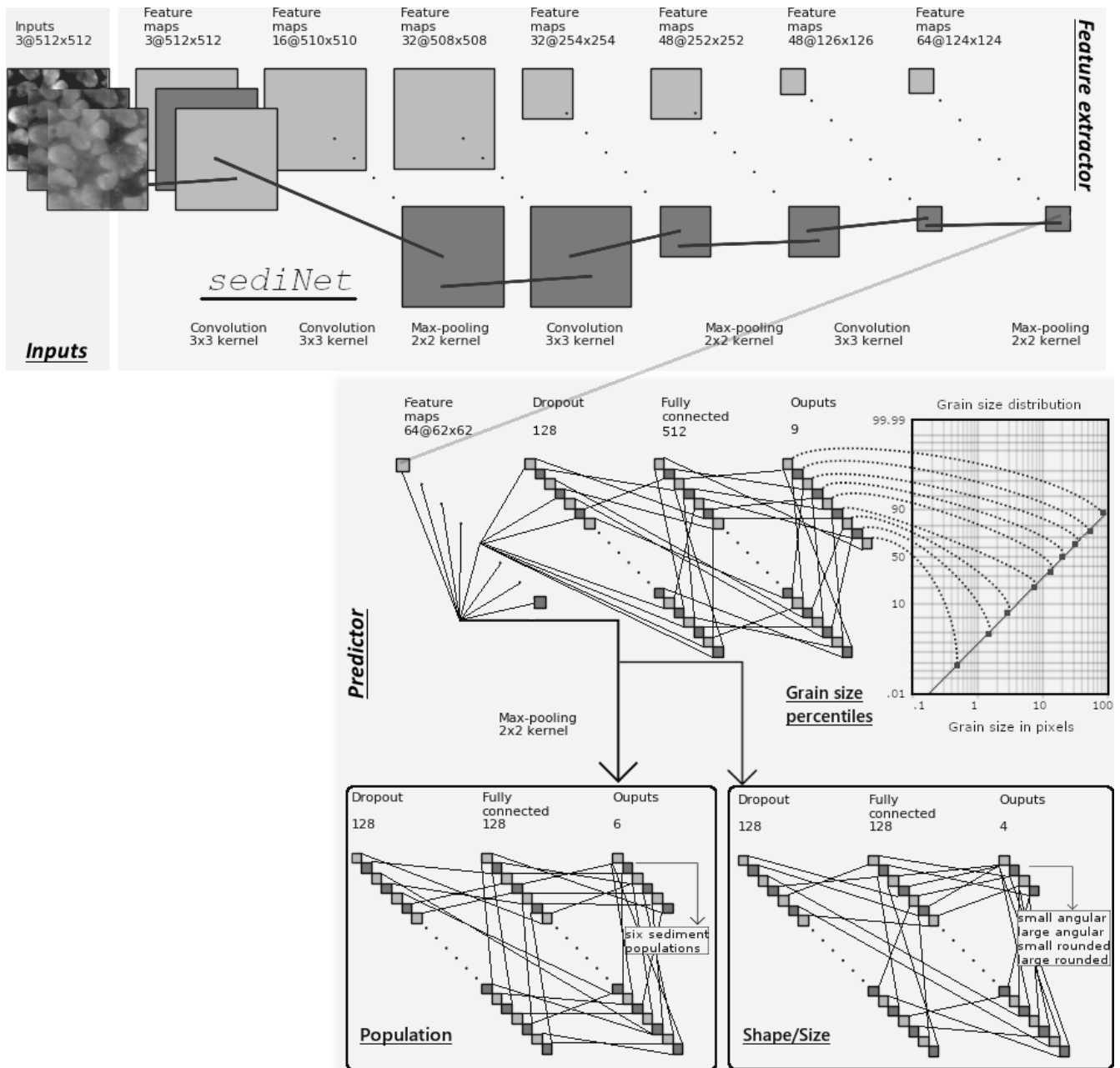
193

- 194 1. To estimate nine percentiles of the cumulative grain size distribution in pixels, trained
195 on 204 images and tested on 205 images, both drawn randomly. The train and test
196 sets consist of images of several populations of grains from a wide sedimentological
197 spectrum
- 198 2. To estimate nine percentiles of the cumulative grain size distribution in pixels, trained
199 on 15 images and tested on 16 images of one population (beach sands)
- 200 3. To estimate sieve size in microns directly, without first estimating the pixel size, trained
201 on the same 15 images and tested on 16 images as above
- 202 4. To estimate six categorical populations of grains, trained on 204 images and tested
203 on 205 images, both drawn randomly
- 204 5. To estimate four categorical grain shape/size classes, trained on 204 images and
205 tested on 205 images, both drawn randomly

206

207 Given the set of n images, let us denote one sample $X_\mu \in \mathbb{R}^p$ with $\mu = 1 \dots n$, where p is the
208 number of pixels. For each sample, X_μ there is label $y_\mu \in \mathbb{R}^q$ where q is the number of
209 combined categorical and continuously distributed classes. Using the deep learning
210 architecture described below, and the training data set $\{X_\mu, y_\mu\}$ consisting of 50 % of the total
211 number of images, randomly selected, a function f is found such that $\hat{y} = f(X)$, where \hat{y} is
212 the predicted set of labels/metrics from sample image X . The remaining 50 % of the total data
213 set was used as a test set to evaluate model performance.

214



215

216 *Figure 3. Schematic of the SediNet architecture, as applied to estimating the grain size distribution, and categorical population and*
 217 *shape/size. An input image is passed to the feature extractor consisting of a series of convolutional blocks. The last set of feature*
 218 *maps, which is the result of the last 2D max global pooling layer, is fed into one of three multi-layer perceptrons; one each for the task*
 219 *of estimating grain size percentiles, sediment population, and grain shape.*

220

221 The image feature extractor consists of four convolutional blocks each consisting of a several
 222 two-dimensional convolutional filter layers, batch normalization layers, and two-dimensional
 223 max pooling layers (Figure 3). Batch normalization applies a transformation that maintains
 224 the mean neuron activation of zero and the activation standard deviation of one (*Ioffe and*
 225 *Szegedy, 2015*). Pooling layers are used to reduce the spatial dimensions of each of the

226 three-dimensional tensors associated with each pixel of the input image, from $h \times w \times d$ to 1
227 $\cdot 1 \times d$, by averaging over h and w . This has the effect of reducing the total number of
228 parameters in the model, thereby minimizing overfitting. The output of the last block is the
229 input of the next. The number of filters increases for each of the four blocks, from 16 in the
230 first block, 32 in the second, 48 in the third and finally 64 in the last block. After the last
231 convolutional block, there is one more batch normalization and two-dimensional max pooling
232 layer, and a dropout layer that randomly drops half the neurons (*Srivastava et al.*, 2014).
233 Batch normalization, max pooling, and dropout layers are techniques to prevent overfitting
234 the model (i.e., memorizing the training data rather than learning a general trend). The
235 extracted feature is fed into a series of multilayer perceptrons, one for each estimated
236 quantity, that each culminates in a dense predicting layer with linear regression (known in
237 machine learning literature as a linear activation function) for continuous variable prediction
238 variables (such as grain size in pixels, or sieve size directly), or multinomial logistic regression
239 (in machine learning parlance, a softmax activation function) for categorical variables such
240 as grain shape and population.

241

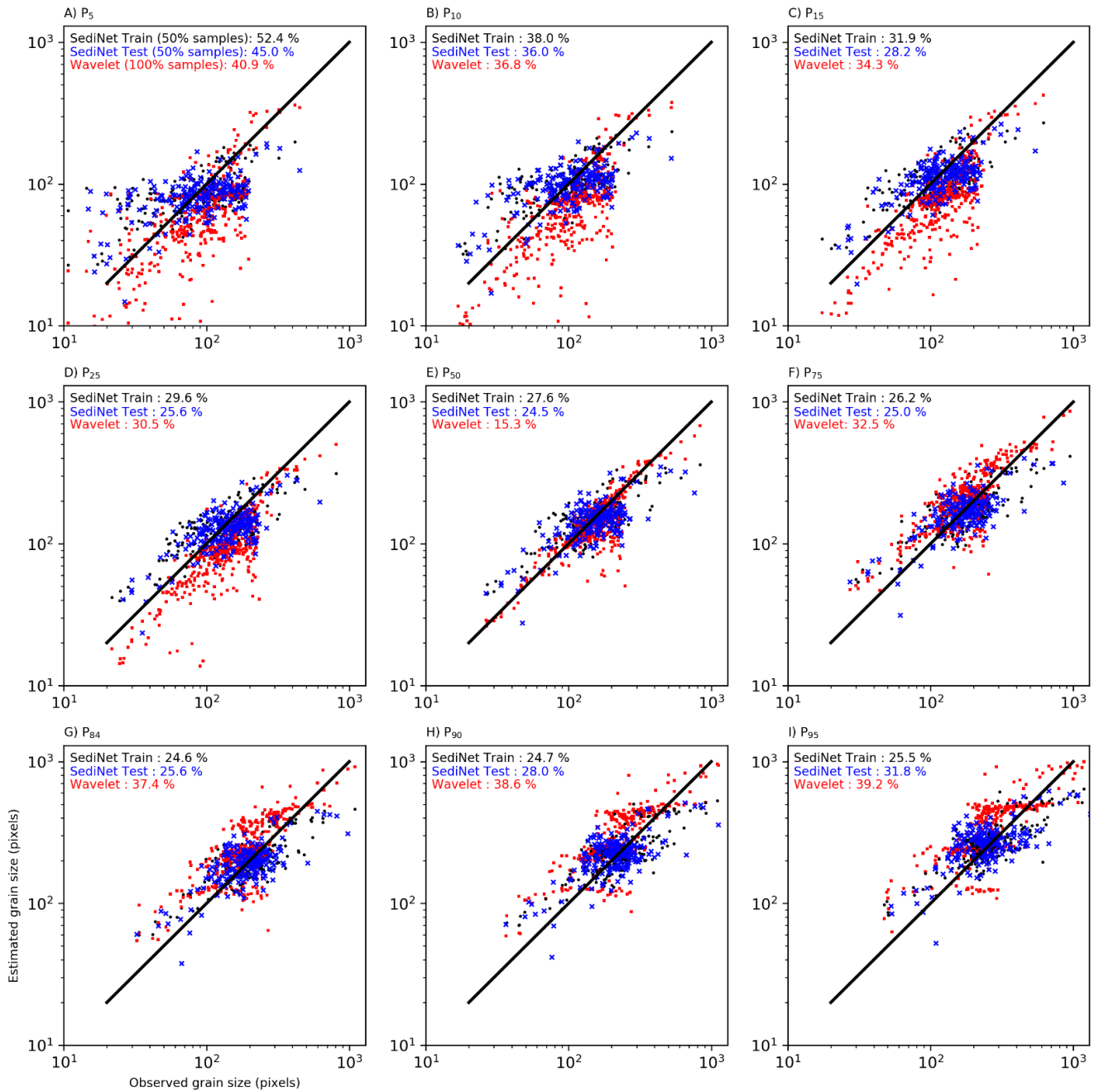
242 The model was retrained 'end-to-end', which means it was initialized with random numbers
243 for neuron weights $w \in \mathbb{R}^k$, then during training the value of those parameters was optimized
244 by minimizing the discrepancy between known and estimated quantities by minimizing a loss
245 function $L[f_w(X_\mu, y_\mu)]$ for each sample μ where f_w denotes weighted function. By doing so,
246 the model simultaneously and automatically learns feature representations from imagery and
247 a mapping from those features to the target values (e.g. grain size) or classes (e.g. grain
248 shape). Models are trained over several epochs. One training epoch means that the learning
249 algorithm has made one pass through the training dataset, where examples were separated
250 into randomly selected batches of images. The number of training steps per epoch was

251 computed as the number of training images divided by the batch size. In this study, the batch
252 size was set to eight and results were not sensitive to its value. Upon each step, the gradients
253 of the network are updated and new weights assigned to each neuron. Stochastic gradient
254 descent was used to iteratively adjusting the weights in the direction of the gradient of the
255 average of the loss over the training set using $w^{t+1} = w^t - \lambda \nabla_w R(f_w)$, where t is iteration
256 number (step within an epoch) and λ is the so-called ‘learning rate’, and where $R(f_w) = \sum L/n$
257 for the full training data is replaced by the contribution of just a few of the samples.

258

259 During model training, each $h \times w \times 3$ pixel input image was resized to $512 \times 512 \times 3$ pixels
260 for computational efficiency. With sufficient computing power, larger images and larger
261 numbers of images could be used. That the image’s aspect ratio is typically not preserved
262 does not affect model performance (I revisit this point in the Discussion). The method was
263 implemented in python 3.7 using the Tensorflow (Abadi et al., 2015) backend to the keras
264 (Chollet et al., 2015) module, on a GeForce RTX 2080Ti GPU with 11 GB of memory. The
265 resolution of a given grain size estimate in pixels is approximately 2 pixels, determined as the
266 range of that variable in the training data (in the present case, the largest grain size minus
267 the smallest, which is approximately 1000 pixels) divided by the number of neurons in the
268 final dense layer, which was set to 512 (Figure 3). Training utilized the popular Adam
269 algorithm (Kingma and Ba, 2014) for stochastic optimization, with parameters $\beta_1 = 0.9$ and
270 $\beta_2 = 0.999$ (Buscombe et al., 2019). During training, λ was automatically reduced when the
271 loss function stabilized, i.e. when its value stopped decreasing, by a factor of 0.8 after 15
272 epochs had elapsed with no improvement (Buscombe et al., 2019). A lower bound on λ was
273 set at 0.0001. The maximum number of training epochs was set to 100. Models stopped
274 training early (i.e. before 100 epochs) if the validation loss failed to improve for 20 consecutive

275 epochs. Models typically trained for between 40 and 100 epochs before the criterion was met
 276 to stop training early.



277

278 *Figure 4. Observed versus estimated grain size percentiles in pixels, for all 409 images. Black dots are the estimate from the training*
 279 *image set (204 samples). Blue crosses are the estimates from the remaining 205 test images. Red dots are all 409 samples analyzed*
 280 *using the wavelet method of Buscombe (2013).*

281

282 4. Results

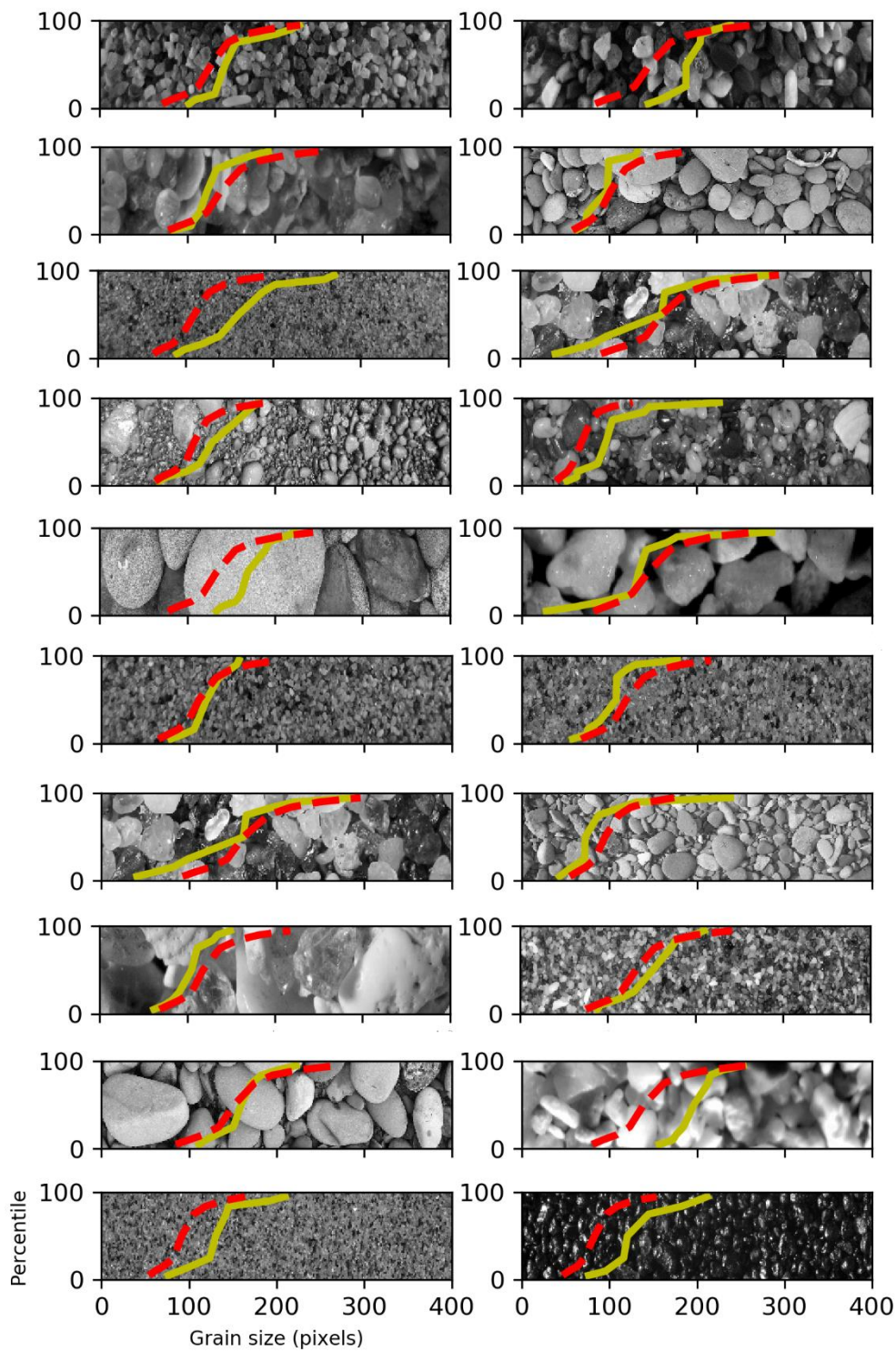
283 4.1. Grain Size

284 The first implementation of SediNet estimated nine percentiles of the cumulative grain size
285 distribution in pixels, trained on 204 images with mean error between 24 and 52% depending
286 on percentile, and tested on 205 images with mean error between 24 and 45% again varying
287 with percentile (Figures 4 and 5). Mean percent error for each percentile is computed as 100
288 times the root-mean-squared error normalized by the mean grain size associated with that
289 percentile. Overall, this SediNet model out-performed the wavelet technique of *Buscombe*
290 (2013) and required fewer tunable parameters.

291

292 The second implementation of SediNet was for estimating nine percentiles of the cumulative
293 grain size distribution in pixels for a smaller population of sediment images from a given
294 environment (Figure 6). I chose a set of 31 images of sieved beach sand, separated into 16
295 test and 15 training images. Mean error on the training set was between 7 and 29%, and
296 between 16 and 29% for the test set (Figure 6, A – I). The third SediNet implementation
297 estimated sieve size directly from the same imagery without first estimating the grain size in
298 pixels. Therefore, it implicitly learned the actual size of an image pixel. This model tended to
299 slightly underestimate grain size, with train and test mean errors of 29 and 22%, respectively.
300 The slight bias in the prediction might be corrected empirically, such as by means of
301 parameter x in equation (1), or through further refinement of the model architecture or training
302 procedure. In all three SediNet grain size models, the mean errors for test and train datasets
303 were similar, strongly indicating that the model has generalized well to the data and has not
304 overfit the training data.

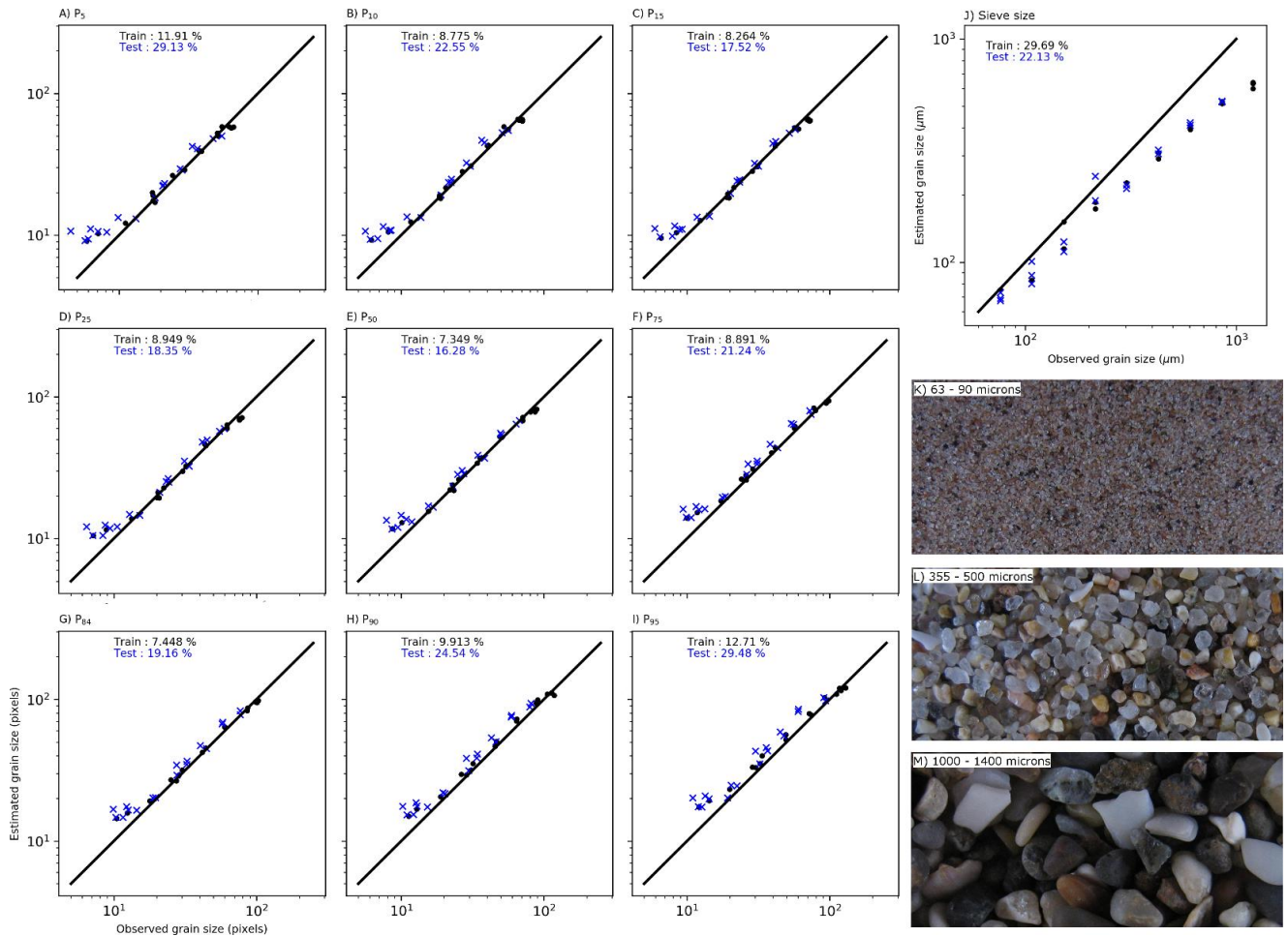
305



306

307 *Figure 5. Example true (solid yellow line) and estimated (dashed red line) cumulative distributions for 20 randomly selected images,*
 308 *small subsets of which are shown in the background of each subplot.*

309



310

311 *Figure 6. Analysis of one sediment population, consisting of 31 images of sieved beach sands from samples taken at Pescadero in*
 312 *California (images courtesy of David Rubin). A – I) Observed versus estimated grain size percentiles in pixels where black dots are the*
 313 *estimate from the training image set (15 samples) and blue crosses are the estimates from the remaining 16 test images.; J) observed*
 314 *versus estimated mid-sieve size, obtained directly from the image without knowledge of the pixel size; and K – M) example images of*
 315 *three sieve fractions.*

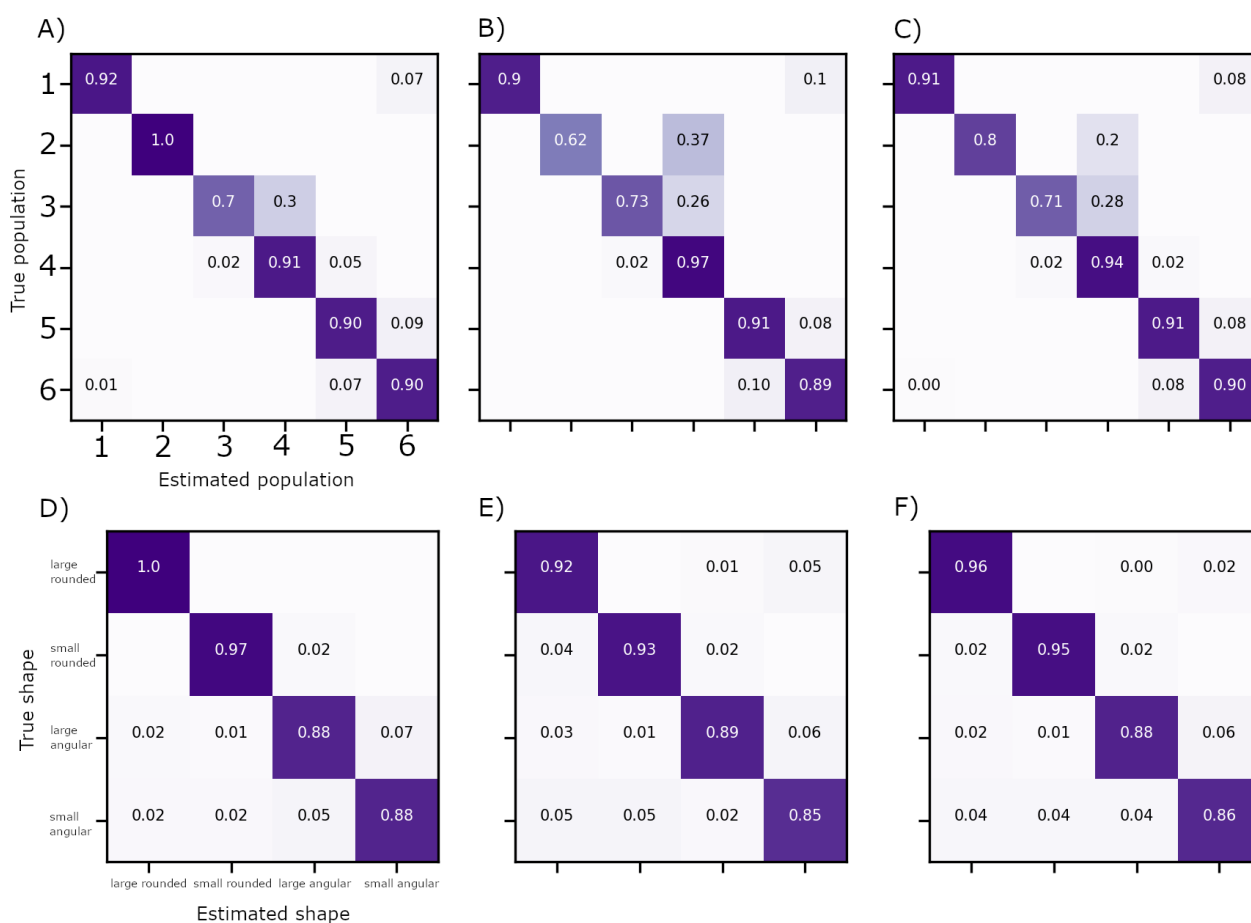
316

317

318 4.2. Grain shape and population

319 The fourth implementation of SediNet estimated six categorical populations of sediment,
 320 trained on 204 images and tested on 205 images, both drawn randomly. Classification skill
 321 was evaluated using a ‘confusion matrix’ of normalised correspondences between true and
 322 estimated labels (Figure 7, A - C). A perfect correspondence between true and estimated
 323 labels is scored 1.0 along the diagonal elements of the matrix. Random misclassifications are
 324 readily identified as off-diagonal elements with relatively small magnitudes, and systematic
 325 misclassifications are recognized as off-diagonal elements with relatively large magnitudes.

326 The three confusion matrices for categorical sediment population shown in Figure 7, A – C
 327 show skill for, respectively, training, testing and combined (i.e. all 400 images) data. The
 328 model overfits population 2 (underwater images of continental shelf sand, Figure 1),
 329 evidenced by the large discrepancy between training skill (1.0) and test skill (0.62; Figure 7A,
 330 B). However, overfitting is not evident for the other five classes, with test scores being
 331 approximately equal to training scores. All classes are classified with accuracies of > 70% for
 332 the combined model (Figure 7C).



333

334 *Figure 7. Confusion matrices for (A – C) categorical population and (D – F) categorical shape. Subplots A and B show training and*
 335 *testing datasets*

336

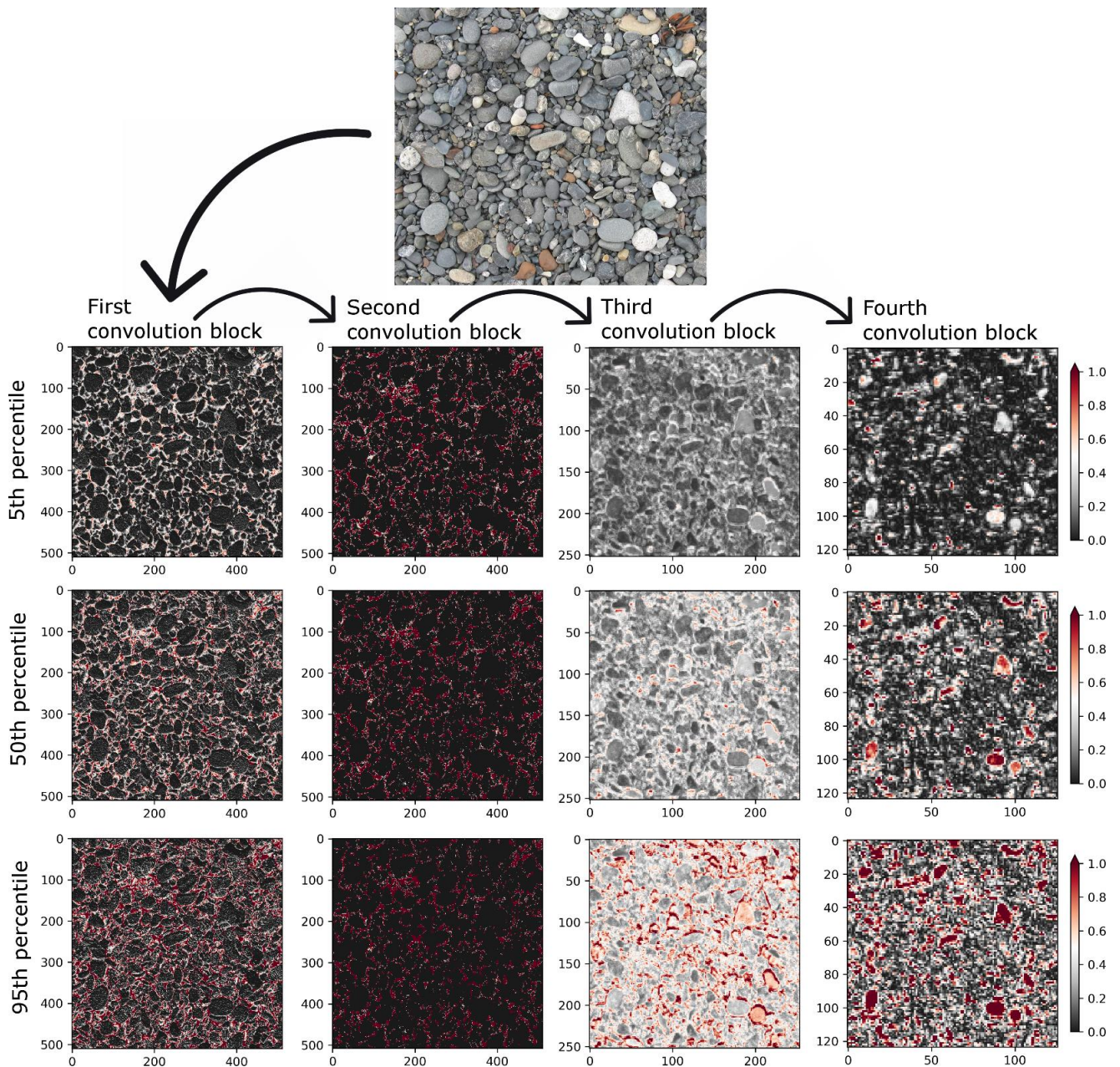
337 The fifth and final SediNet implementation reported here was configured to estimate four
 338 categorical grain shape/size classes, trained on 204 images and tested on 205 images, both
 339 drawn randomly. The three confusion matrices for categorical sediment shape shown in

340 Figure 7D – F show skill for, respectively, training, testing and combined (i.e. all 400 images)
341 data. The similarity in train and test scores for all four classes demonstrates the model has
342 not overfit the data. All classes are classified with accuracies of > 85% for the test, train and
343 combined models (Figure 7D - F).

344

345 5. Discussion

346 The task of quantifying and classifying natural objects and textures in images of sedimentary
347 landforms is increasingly widespread in a wide variety of geomorphological research
348 (*Franklin and Mulder, 2002; Mulder et al., 2011; Smith and Pain, 2009*), especially as imagery
349 collection using UAVs becomes more prevalent (*Carbonneau et al., 2018; Gomez and*
350 *Purdie, 2016; Turner et al., 2016*). The automated method to size and classify sediment
351 described here could maximize speed and objectivity of sedimentary description at large
352 scales, and might be applied to the analysis of datasets consisting of tens to millions of
353 individual images. The model framework could enable spatio-temporal monitoring of grain
354 size more efficiently, being configurable to estimate many custom-defined quantities and
355 qualities for specific tasks. Given it is a data-driven approach, models trained for use in
356 specific environments will highly likely be as or more accurate than methods such as
357 *Buscombe (2013)* and *Carbonneau et al., (2004)* that are based on signal processing or
358 random field theory, especially for poorly sorted sediment, small field-of-view, and large grain
359 size compared to field-of-view (small numbers of individual grains). This is because those
360 methods are not informed by data (i.e. only tested with data); therefore, the massive variation
361 in natural sediment can only be a limitation in their application.



362

363 *Figure 8. Activation map outputs from each of the four convolutional blocks (columns) in the SediNet model, for three grain size*
 364 *percentiles (rows) for an example image of gravels. Red areas indicate relatively high activation values.*

365

366 The success of the SediNet approach using images resized to 512 x 512 x 3 pixels,
 367 irrespective of original size that was typically much larger, reveals two interesting
 368 phenomena. First, an image's aspect ratio does not need to be preserved to provide an
 369 accurate grain size, shape or population estimate. Second, those quantities can be estimated
 370 even with many subpixel grains, which is the case for relatively fine grains and/or images that
 371 have undergone a relatively large amount of downsizing. This is because the model learns

372 which textures are associated with each grain size, at the scale of imagery provided but
373 regardless of the scale and distortion of pixels. Therefore, the use of the model requires all
374 input imagery to be the same size as that used to train the model. This observation bodes
375 well for applications of this or similar technique on aerial or satellite imagery of sedimentary
376 deposits where most grains exist at subpixel scales, but where spatial resolution is sufficient
377 to create images textures uniquely diagnostic of grain size. Optical granulometry methods
378 similar to *Carbonneau et al. (2004)* operate under the same principles, except in those
379 methods image features are extracted using prescribed filters (and their hyperparameters)
380 such as entropy (and kernel size) rather than those features extracted through an iterative
381 procedure that is optimized to minimize observation-estimate error.

382

383 It is useful to visualize which parts of a given image led the model to its final decision. Class
384 Activation Map (CAM) visualization (*Selvaraju et al., 2017*) consists of computing 2D grids of
385 scores associated with a specific output value (such as a specific grain size), computed for
386 every location in any input image, indicating how important each location is with respect to
387 the output value. The “gradCAM” technique of *Selvaraju et al., (2017)* computes the partial
388 differentiation of the predicted output with respect to each channel in a previous layer (the
389 layer for which we want visualize CAMs). The gradient of the resulting activations are scores
390 of how important each channel is for the predicted output, which when multiplied by said
391 channels acts to weigh each channel responsible for the predicted output. The weighted
392 channel-wise mean is the CAM. I implemented this technique by computing the gradient of
393 an image’s estimated grain size with regard to the output feature map of each of the four
394 convolutional blocks in the SediNet grain-size model (Figure 3). Then I computed the product
395 of 1) the mean of the gradient over each feature map channel and 2) each channel in the
396 feature map. Finally, the channel-wise mean of the resulting feature map is our 2D heatmap

397 of class activation scores. Figure 8 exemplifies this for one example image and the model-
398 estimated grain size associated with the 5th, 50th, and 95th percentiles of the cumulative grain
399 size distribution (rows in Figure), showing CAMs for all four convolution blocks in the SediNet
400 grain-size model (Figure columns). One might interpret each of these 12 CAMs as a spatial
401 map of how intensely the input image activates a specific grain size value, achieved by
402 weighting a spatial map of how intensely the input image activates different channels in the
403 convolutional block by another spatial map of how important each channel is with regard to
404 the grain size value. The analysis demonstrates that each convolution block is weighted to
405 activate different parts of the input image (Figure 8A). The first and second convolutional
406 blocks tend to result in activations in grain interstices only, with generally stronger activations
407 for larger percentiles (compare Figure 8B and 8J, and 8C and 8K). The third and fourth
408 convolution block results in stronger activations for individual grains and grain outlines with
409 generally stronger activations for larger percentiles and for the largest grains (compare Figure
410 8E and 8M).

411

412 Convolutional neural networks have been particularly useful for analysis of images because
413 they implement invariance to translation and the convolution filters share weights spatially,
414 which exploits stationarity in the image (*Buscombe and Carini, 2019; Goodfellow et al., 2016*).
415 There is typically a lot of stationarity (i.e. repeating spatial patterns) in images of sediment
416 grains, because the location of grains of all sizes within the image is typically random. This
417 is especially the case for relatively well-sorted sediment and or images of relatively large
418 numbers of individual grains, because in those cases grains of all sizes are present in large
419 numbers throughout the image. Training a deep neural network requires fitting a large
420 number of parameters, which usually requires large training datasets. This paper has
421 demonstrated that 400 images might be a sufficiently large data set to train a model that

422 produces accurate predictions on unseen test images, but I would expect models only to
423 improve by retraining and refining with more data. Data-driven models should also be highly
424 accurate for smaller populations given large training data (Figure 6). Another approach to
425 mitigating any reliance on large datasets is to use simulations to generate supplemental
426 synthetic training data (e.g. *Buscombe, 2013; Buscombe and Rubin, 2012a*) or using data
427 augmentation through random image synthesis (e.g. *Buscombe et al., 2019*). Given recent
428 progress in self-supervised deep learning models that do not require data labeling (e.g. *Oh*
429 *et al., 2019*), it might even soon be possible to estimate sedimentological quantities
430 accurately without manual image classification, manual axes measurements, or some other
431 form of calibration.

432

433 Conclusions

434 I have described a configurable machine-learning framework called SediNet for estimating
435 either (or both) continuous and categorical variables from a photographic image of clastic
436 sediment. To demonstrate the framework, five separate models were configured and trained,
437 three of which for estimating various grain size metrics on both mixed and single populations
438 of sediment, and two for classifying aspects of grain shape and population. Perhaps of most
439 significance is that SediNet can be configured and trained to estimate equivalent sieve
440 diameters directly from image features, without the need for area-to-mass conversion
441 formulas and without even knowing the scale of one pixel. As such, it is the only optical
442 granulometry method proposed to date that does not necessarily require image scaling.
443 SediNet will allow for reliable estimation of several sedimentological variables from arbitrary
444 imagery of sediment, where grains may be either supra- or sub-pixel in scale, and where
445 conversions between grain size measurements on different physical or statistical scales
446 might be learnt directly from the data. The model framework should therefore find numerous

447 application in the spatio-temporal monitoring of the grain size distribution, shape, mineralogy
448 and other quantities of interest, of sedimentary deposits as they evolve. This study has also
449 served to exemplify how machine learning can be a powerful tool for automated and
450 simultaneous quantitative and qualitative measurements from the same remotely sensed
451 imagery.

452

453 Acknowledgments

454 This work is fully reproducible using data and code at
455 <https://github.com/MARDAScience/SediNet>, which also includes further examples of how to
456 configure SediNet for different purposes.

457

458 References

- 459 1. Abadi M.; Agarwal A.; Barham P.; Brevdo E.; Chen Z.; and 35 others. 2015.
460 *TensorFlow: Large-scale machine learning on heterogeneous systems*. Software
461 available online: <https://www.tensorflow.org> (accessed on 1 July, 2019).
- 462 2. Adams J. 1979. Gravel size analysis from photographs. *Journal of the Hydraulics*
463 *Division. American Society of Civil Engineers*: 1247–1255.
- 464 3. Austin, M.J., Masselink, G., O'Hare, T.J. and Russell, P.E. 2007. Relaxation time
465 effects of wave ripples on tidal beaches. *Geophysical Research Letters*, 34(16).
- 466 4. Baptista, P., Cunha, T., Gama, C., and Bernardes, C. 2012. A new and practical
467 method to obtain grain size measurements in sandy shores based on digital image
468 acquisition and processing. *Sedimentary Geology*, 282, 294–306.
- 469 5. Barnard, P., Rubin, D., Harney, J., and Mustain, N. 2007. Field test comparison of an
470 autocorrelation technique for determining grain size using a digital beachball camera
471 versus traditional methods. *Sedimentary Geology*, 201 (1-2), 180–195.

- 472 6. Bergillos, R.J., Ortega-Sánchez, M., Masselink, G. and Losada, M.A. 2016. Morpho-
473 sedimentary dynamics of a micro-tidal mixed sand and gravel beach, Playa Granada,
474 southern Spain. *Marine Geology*, 379, 28-38.
- 475 7. Black, M., Carbonneau, P., Church, M., and Warburton, J. 2014. Mapping sub-pixel
476 fluvial grain sizes with hyperspatial imagery. *Sedimentology*, 61 (3), 691–711.
- 477 8. Buscombe, D. 2013. Transferable wavelet method for grain-size distribution from
478 images of sediment surfaces and thin sections, and other natural granular patterns.
479 *Sedimentology*, 60 (7), 1709–1732.
- 480 9. Buscombe, D., and Carini, R. J. 2019. A data-driven approach to classifying wave
481 breaking in infrared imagery. *Remote Sensing*, 11 (7), 859.
- 482 10. Buscombe, D., Carini, R., Harrison, S., Chickadel, C., and Warrick, J. 2019. Optical
483 wave gauging with deep neural networks. *Coastal Engineering*, in review July 2019
- 484 11. Buscombe, D. and Masselink, G. 2006. Concepts in gravel beach dynamics. *Earth-*
485 *Science Reviews*, 79 (1-2), 33-52.
- 486 12. Buscombe, D. and Ritchie, A. 2018. Landscape classification with deep neural
487 networks. *Geosciences*, 8 (7), 244.
- 488 13. Buscombe, D., and Rubin, D. M. 2012a. Advances in the simulation and automated
489 measurement of well-sorted granular material: 1. Simulation. *Journal of Geophysical*
490 *Research: Earth Surface*, 117 (F2).
- 491 14. Buscombe, D., and Rubin, D. M. 2012b. Advances in the simulation and automated
492 measurement of well-sorted granular material: 2. Direct measures of particle
493 properties. *Journal of Geophysical Research: Earth Surface*, 117 (F2).
- 494 15. Buscombe, D., Rubin, D. M., Lacy, J. R., Storlazzi, C. D., Hatcher, G., Chezar, H., and
495 Sherwood, C. R. 2014. Autonomous bed-sediment imaging-systems for revealing

- 496 temporal variability of grain size. *Limnology and Oceanography: Methods*, 12 (6), 390–
497 406.
- 498 16. Buscombe, D., Rubin, D., and Warrick, J. 2010. A universal approximation of grain
499 size from images of noncohesive sediment. *Journal of Geophysical Research: Earth*
500 *Surface*, 115 (F2).
- 501 17. Carbonneau, P., Bizzi, S., and Marchetti, G. 2018. Robotic photosieving from low-cost
502 multicopter sUAS: A proof-of-concept. *Earth Surface Processes and Landforms*, 43 (5),
503 1160–1166.
- 504 18. Carbonneau PE, Bergeron N, Lane SN. 2005a. Automated grain size measurements
505 from airborne remote sensing for long profile measurements of fluvial grain sizes.
506 *Water Resources Research*: 41.
- 507 19. Carbonneau PE, Bergeron NE, Lane SN. 2005b. Texture-based image segmentation
508 applied to the quantification of superficial sand in salmonid river gravels. *Earth Surface*
509 *Processes and Landforms* 30: 121–127.
- 510 20. Carbonneau, P.E., Lane, S.N. and Bergeron, N.E. 2004. Catchment-scale mapping of
511 surface grain size in gravel bed rivers using airborne digital imagery. *Water Resources*
512 *Research*, 40 (7).
- 513 21. Chollet, F. 2015. Keras. Software available online: <https://keras.io> (accessed on 1 July,
514 2019).
- 515 22. Cheng, Z. and Liu, H. 2015. Digital grain-size analysis based on autocorrelation
516 algorithm. *Sedimentary Geology*, 327, 21-31.
- 517 23. Cuttler, M. V., Lowe, R. J., Falter, J. L., and Buscombe, D. 2017. Estimating the settling
518 velocity of bioclastic sediment using common grain-size analysis techniques.
519 *Sedimentology*, 64 (4), 987–1004.

- 520 24. Detert M, Weitbrecht V. 2012. Automatic object detection to analyze the geometry of
521 gravel grains – a free stand-alone tool. In River Flow, 2012, Munoz RM (ed). CRC
522 Press: London; 595–600.
- 523 25. Diplas, P. and Fripp, J.B. 1992. Properties of various sediment sampling procedures.
524 *Journal of Hydraulic Engineering*, 118, 955–970.
- 525 26. Diplas, P., Kuhnle, R.A., Gray, J.R., Glysson, G.D. and Edwards, T.E. 2008.
526 Sediment transport measurements. In: Sedimentation Engineering: Processes,
527 Measurements, Modeling, and Practice (Ed. M.H. Garcia), 110, 307–353. American
528 Society of Civil Engineering Manuals and Reports on Engineering Practice, Reston,
529 VA
- 530 27. Diplas, P. and Sutherland, A.J. 1988. Sampling techniques for gravel sized sediments.
531 *Journal of Hydraulic Engineering*, 114, 484–501.
- 532 28. Dugdale, S. J., Carbonneau, P. E., and Campbell, D. 2010. Aerial photosieving of
533 exposed gravel bars for the rapid calibration of airborne grain size maps. *Earth Surface*
534 *Processes and Landforms*, 35 (6), 627–639.
- 535 29. Franklin, S., and Wulder, M. 2002. Remote sensing methods in medium spatial
536 resolution satellite data land cover classification of large areas. *Progress in Physical*
537 *Geography*, 26 (2), 173–205.
- 538 30. Gomez, C., and Purdie, H. 2016. UAV-based photogrammetry and geocomputing for
539 hazards and disaster risk monitoring—A review. *Geoenvironmental Disasters*, 3 (1), 23.
- 540 31. Goodfellow, I., Bengio, Y., Courville, A., and Bengio, Y. 2016. *Deep learning* (Vol. 1).
541 MIT press Cambridge.
- 542 32. Graham DJ, Reid I, Rice SP. 2005. Automated sizing of coarse-grained sediments:
543 image-processing procedures. *Mathematical Geology* 37: 1–28.
- 544 33. Graham, D., Rollet, A., Rice, S., and Piegay, H. 2012. Conversions of surface grain-
545 size samples collected and recorded using different procedures. *Journal of Hydraulic*
546 *Engineering*, 138 (10), 839–849.

- 547 34. Ioffe, S., and Szegedy, C. 2015. Batch normalization: Accelerating deep network
548 training by reducing internal covariate shift. *arXiv preprint arXiv:1502.03167*.
- 549 35. Jiang, G.-Q., Xu, J., and Wei, J. 2018. A deep learning algorithm of neural network for
550 the parameterization of typhoon-ocean feedback in typhoon forecast models.
551 *Geophysical Research Letters*, 45 (8), 3706–3716.
- 552 36. Kellerhals, R., and Bray, D. I. 1971. Sampling procedures for coarse fluvial sediments.
553 *Journal of the Hydraulics Division*, 97 (8), 1165–1180.
- 554 37. Kingma, D. P., and Ba, J. 2014. Adam: A method for stochastic optimization.
555 *arXiv preprint arXiv:1412.6980*.
- 556 38. Legleiter, C.J., Stegman, T.K. and Overstreet, B.T. 2016. Spectrally based mapping
557 of riverbed composition. *Geomorphology*, 264, 61-79.
- 558 39. Linville, L., Pankow, K., and Draelos, T. 2019. Deep learning models augment analyst
559 decisions for event discrimination. *Geophysical Research Letters*, 46 (7), 3643–3651.
- 560 40. Luo, J. Y., Irisson, J.-O., Graham, B., Guigand, C., Sarafraz, A., Mader, C., and
561 Cowen, R. K. 2018. Automated plankton image analysis using convolutional neural
562 networks. *Limnology and Oceanography: Methods*, 16 (12), 814–827.
- 563 41. Masteller, C.C. and Finnegan, N.J. 2017. Interplay between grain protrusion and
564 sediment entrainment in an experimental flume. *Journal of Geophysical Research:
565 Earth Surface*, 122 (1), 274-289.
- 566 42. Michaelides, K., Hollings, R., Singer, M.B., Nichols, M.H. and Nearing, M.A. 2018.
567 Spatial and temporal analysis of hillslope–channel coupling and implications for the
568 longitudinal profile in a dryland basin. *Earth Surface Processes and Landforms*, 43 (8),
569 1608-1621.
- 570 43. Montgomery, D. R., Panfil, M. S., and Hayes, S. K. 1999. Channel-bed mobility
571 response to extreme sediment loading at Mount Pinatubo. *Geology*, 27 (3), 271–274.

- 572 44. Mulder, V., De Bruin, S., Schaepman, M., and Mayr, T. 2011. The use of remote
573 sensing in soil and terrain mapping: A review. *Geoderma*, 162 (1-2), 1–19.
- 574 45. Nield, J.M., Wiggs, G.F. and Squirrell, R.S. 2011. Aeolian sand strip mobility and
575 protodune development on a drying beach: examining surface moisture and surface
576 roughness patterns measured by terrestrial laser scanning. *Earth Surface Processes
577 and Landforms*, 36 (4), 513-522.
- 578 46. Novak-Szabo, T., Sipos, A.A., Shaw, S., Bertoni, D., Pozzebon, A., Grottoli, E.,
579 Jerolmack, D. J. 2018. Universal characteristics of particle shape evolution by bed-
580 load chipping. *Science Advances*, 4 (3).
- 581 47. Oh, C., Ham, B., Kim, H., Hilton, A. and Sohn, K. 2019. OCEAN: Object-centric
582 arranging network for self-supervised visual representations learning. *Expert Systems
583 with Applications*, 125, 281-292.
- 584 48. Paterson, G. A., and Heslop, D. 2015. New methods for unmixing sediment grain size
585 data. *Geochemistry, Geophysics, Geosystems*, 16 (12), 4494–4506.
- 586 49. Pfeiffer, A. M., Finnegan, N. J., and Willenbring, J. K. 2017. Sediment supply controls
587 equilibrium channel geometry in gravel rivers. *Proceedings of the National Academy
588 of Sciences*, 114 (13), 3346–3351.
- 589 50. Prodger, S., Russell, P., Davidson, M., Miles, J. and Scott, T. 2016. Understanding
590 and predicting the temporal variability of sediment grain size characteristics on high-
591 energy beaches. *Marine Geology*, 376, 109-117.
- 592 51. Reichstein, M., Camps-Valls, G., Stevens, B., Jung, M., Denzler, J., Carvalhais, N.
593 2019. Deep learning and process understanding for data-driven Earth system science.
594 *Nature*, 566 (7743), 195.
- 595 52. Rickenmann, D., and Recking, A. 2011. Evaluation of flow resistance in gravel-bed
596 rivers through a large field data set. *Water Resources Research*, 47 (7).

- 597 53. Rubin, D. 2004. A simple autocorrelation algorithm for determining grain size from
598 digital images of sediment. *Journal of Sedimentary Research*, 74 (1), 160–165.
- 599 54. Rubin, D., Buscombe, D., Wright, S., Topping, D., Grams, P., and Schmidt, J. 2019.
600 What grain size reveals about suspended-sand transport in the Colorado River in
601 Grand Canyon. *Journal of Geophysical Research - Earth Surface*, in review.
- 602 55. Rubin, D., Chezar, H., Harney, J., Topping, D., Melis, T., and Sherwood, C. 2007.
603 Underwater microscope for measuring spatial and temporal changes in bed-sediment
604 grain size. *Sedimentary Geology*, 202 (3), 402–408
- 605 56. Sedinet online software. 2019. <https://github.com/MARDAScience/SediNet>
- 606 57. Selvaraju, R.R., Cogswell, M., Das, A., Vedantam, R., Parikh, D. and Batra, D. 2017.
607 Grad-cam: Visual explanations from deep networks via gradient-based localization. In:
608 *Proceedings of the IEEE International Conference on Computer Vision*, 618-626.
- 609 58. Shoji, D., Noguchi, R., Otsuki, S. and Hino, H. 2018. Classification of volcanic ash
610 particles using a convolutional neural network and probability. *Scientific Reports*, 8 (1),
611 8111.
- 612 59. Smith, M., and Pain, C. 2009. Applications of remote sensing in geomorphology.
613 *Progress in Physical Geography*, 33 (4), 568–582.
- 614 60. Smith, M.E., Werner, S.H., Buscombe, D., Finnegan, N.J., Sumner, E.J. and Mueller,
615 E.R. 2018. Seeking the shore: Evidence for active submarine canyon head incision
616 due to coarse sediment supply and focusing of wave energy. *Geophysical Research*
617 *Letters*, 45 (22), 12-403.
- 618 61. Srivastava, N., Hinton, G., Krizhevsky, A., Sutskever, I., and Salakhutdinov, R. 2014.
619 Dropout: a simple way to prevent neural networks from overfitting. *The Journal of*
620 *Machine Learning Research*, 15 (1), 1929–1958.

- 621 62. Sternberg, R.W., Berhane, I. and Ogston, A.S. 1999. Measurement of size and settling
622 velocity of suspended aggregates on the northern California continental shelf. *Marine*
623 *Geology*, 154 (1-4), 43-53.
- 624 63. Turner, I. L., Harley, M. D., and Drummond, C. D. 2016. UAVs for coastal surveying.
625 *Coastal Engineering*, 114, 19–24.
- 626 64. Turner, I.L., Russell, P.E. and Butt, T. 2008. Measurement of wave-by-wave bed-
627 levels in the swash zone. *Coastal Engineering*, 55 (12), 1237-1242.
- 628 65. Viles, H. 2016. Technology and geomorphology: Are improvements in data collection
629 techniques transforming geomorphic science? *Geomorphology*, 270, 121–133.
- 630 66. Warrick, J.A., Rubin, D.M., Ruggiero, P., Harney, J.N., Draut, A.E. and Buscombe, D.
631 2009. Cobble Cam: Grain-size measurements of sand to boulder from digital
632 photographs and autocorrelation analyses. *Earth Surface Processes and Landforms*,
633 34 (13), 1811-1821.
- 634 67. Wheatcroft, R.A. and Borgeld, J.C. 2000. Oceanic flood deposits on the northern
635 California shelf: large-scale distribution and small-scale physical properties.
636 *Continental Shelf Research*, 20 (16), 2163-2190.
- 637 68. Williams, R.D., Brasington, J., Vericat, D. and Hicks, D.M. 2014. Hyperscale terrain
638 modelling of braided rivers: fusing mobile terrestrial laser scanning and optical
639 bathymetric mapping. *Earth Surface Processes and Landforms*, 39 (2), 167-183.
- 640 69. Woodget, A., and Austrums, R. 2017. Subaerial gravel size measurement using topo-
641 graphic data derived from a UAV-SfM approach. *Earth Surface Processes and*
642 *Landforms*, 42 (9), 1434–1443.
- 643 70. Woodget, A., Fyffe, C., and Carbonneau, P. 2018. From manned to unmanned aircraft:
644 Adapting airborne particle size mapping methodologies to the characteristics of sUAS
645 and SfM. *Earth Surface Processes and Landforms*, 43 (4), 857–870.